


Quantum anomalous Hall effect in an antiferromagnetic monolayer of MoOBin Wu , Yong-liang Song, Wei-xiao Ji, Pei-ji Wang, Shu-feng Zhang,^{*} and Chang-wen Zhang[†]
School of Physics and Technology, University of Jinan, Jinan, Shandong 250022, China (Received 10 December 2022; revised 24 April 2023; accepted 6 June 2023; published 13 June 2023)

The quantum anomalous Hall (QAH) effect is rarely predicted in antiferromagnetic (AFM) materials. Here, by first-principles calculations, we propose that the monolayer of MoO is AFM and can be tuned to be a QAH insulator with a band gap of 50 meV. The MoO monolayer is a tetragonal lattice and we have checked its stability by the phonon spectrum and molecular dynamical simulation. It has a collinear AFM order with magnetic moments larger than $2\mu_B$ on each Mo atom. In the absence of strain, it is an AFM metal with a direct gap if spin-orbital coupling is considered. Tensile strain results in a metal-insulator phase transition, but it is still topologically trivial protected by an effective time-reversal symmetry. Shear strain breaks this symmetry and leads to the expected nontrivial electronic bands with Chern number $C = -1$. In addition, its Néel temperature could be larger than room temperature, providing another platform for the application of AFM materials in spintronic devices.

DOI: [10.1103/PhysRevB.107.214419](https://doi.org/10.1103/PhysRevB.107.214419)**I. INTRODUCTION**

The quantum anomalous Hall (QAH) effect is a quantized version of an anomalous Hall effect in the absence of magnetic field [1,2]. It originates from dissipationless chiral edge states which correspond to the topologically nontrivial bulk states with a nonvanishing Chern number [3]. The QAH effect was first predicted by Haldane in a toy model with staggered flux [4]. It indicates that breaking time-reversal symmetry (TRS) is essential for the QAH effect, whether it is due to an external magnetic field or intrinsic magnetism. Since then, the QAH effect has become one of the hot spots for research [5–19].

However, it was only after the discovery of topological insulators [20,21] (TIs) that there appeared an ideal platform to measure the QAH effect. It has been proposed that the QAH effect can be realized by introducing magnetism into TIs [22,23]. So far, the QAH effect has been experimentally verified in three different systems, which are TI films with magnetic dopants [24], MnBi_2Te_4 [25], and moiré superlattice systems formed by magic-angle twisted bilayer graphene [26] or transition metal dichalcogenides [27]. We note that in all three of these systems, TRS is broken by ferromagnetism, which is susceptible to stray fields and has a very low critical temperature for observing a quantized Hall plateau.

Antiferromagnetism can also break TRS and provide an alternative pathway to realizing the QAH effect. Comparing with ferromagnetic insulators, AFM insulators are abundant in the natural world and they are robust to external magnetic perturbations, and have high critical temperatures and a high response frequency [28–30]. Due to these advantages, AFM materials have great potential applications in spintronics. Therefore, achieving the QAH effect in AFM materials

represents a significant theoretical and practical challenge. Experimental reports of AFM QAH insulators are lacking. So far, theoretical calculations have only predicted a few candidate materials such as CrO [31]. The CrO monolayer is an AFM material that becomes a QAH insulator under shear strain, but possesses a tiny band gap of 1 meV. Li *et al.* [32] proposed a strategy to engineer the AFM QAH effect, by considering models of two-dimensional (2D) perovskite layers with strong SOC that isolates an effective total angular momentum $j = 1/2$ subspace of the t_{2g} manifold. Jiang *et al.* [33] investigated the topological properties of the Kane-Mele model as a function of the inversion-breaking ionic potential and the Hubbard interaction. They proposed a AFM Chern insulator phase and a spin-flop transition to a topologically trivial in-plane collinear antiferromagnet. Therefore, it is essential to predict a stable AFM QAH insulator with a large gap.

In this paper, we have predicted another AFM material to realize the QAH effect by first-principles calculations. Our studies show that the square lattice of the MoO monolayer is a collinear AFM metal. But it becomes a QAH insulator if it is tuned by both tensile strain and shear strain. We have checked the stability of this crystal by both the phonon spectrum and molecular dynamics. The Néel temperature of the magnetic phase transition is even larger than 1000 K, as given by the classical Monte Carlo simulation. It suggests that the QAH effect may be measured at a high temperature in experiment. Here, we underline that shear strain may be a possible method to break the effective TRS and leads to a nontrivial phase in AFM materials.

II. METHODS

First-principles calculations have been performed using the Vienna *ab initio* simulation package (VASP), which is based on density functional theory (DFT) [34–36]. The Perdew-Burke-

^{*}sps_zhangsf@ujn.edu.cn[†]ss_zhangchw@ujn.edu.cn

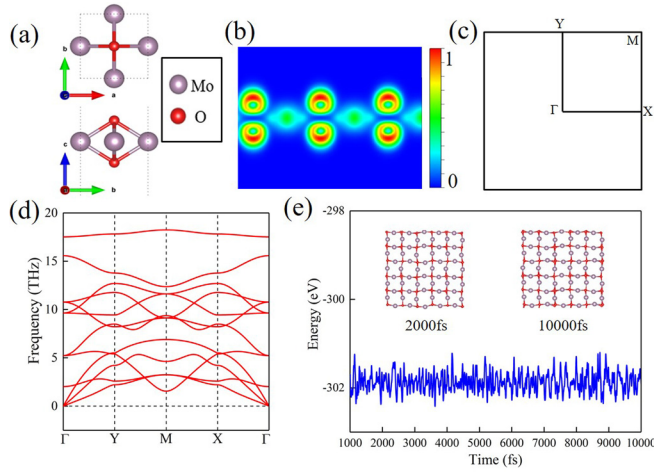


FIG. 1. (a) Top view and side view of the lattice structure (red O atoms, gray Mo atoms). (b) Electron localization function (ELF) in the xOz plane. (c) Schematic diagram of the first Brillouin zone. (d) Phonon spectra. (e) Molecular dynamics simulation.

Ernzerhof functional at the level of generalized gradient approximation (GGA) is used to deal with the exchange-correlation interactions [37]. The correlation effect for the Mo $4d$ electrons is treated by the DFT + U method [38,39] with $U = 2.4$ eV [40]. The plane-wave basis is used with a cutoff energy of 520 eV. The Brillouin zone is sampled with a Γ -centered k mesh of size $15 \times 15 \times 1$. The crystal structure is fully optimized until the force applied on each atom is less than 0.001 eV/Å. The energy convergence criterion is set to be 10^{-8} eV. A vacuum layer of 20 Å is used to avoid residual interactions between neighboring layers. The Berry curvature of occupied bands is calculated by the WANNIERTOOLS software package [41] and the topological edge states are calculated by the WANNI90 software package [42] with the iterative Green's function approach [43].

III. STRUCTURE AND MAGNETISM

The lattice structure of the MoO monolayer is shown in Fig. 1(a) from both a top view and a side view. The red and gray represent the oxygen and molybdenum atoms, respectively. It is clear that there are two Mo and two O atoms in a unit cell. The MoO monolayer is a tetragonal crystal with a relaxed lattice constant of 3.66 Å and the schematic diagram of the first Brillouin zone is given in Fig. 1(c). The corresponding space group is $P4/mmm$, which is a simple space group with point group D_{4h} . To demonstrate the bonding character, we plot its electron localization function (ELF) in Fig. 1(b), in which the electrons are virtually localized over the O and Mo atoms, indicating that the MoO monolayer is a typical ionic crystal.

To confirm the stability of this structure, we have investigated the kinetic, thermodynamic, and mechanical stability of the structure, respectively. At first, we calculate the phonon spectrum of the structure, which is shown in Fig. 1(d). We find that there is no imaginary frequency, which indicates that this structure is kinetically stable. In addition, the phonon spectrum of the structure with $U = 0$ eV is shown in Fig. S1

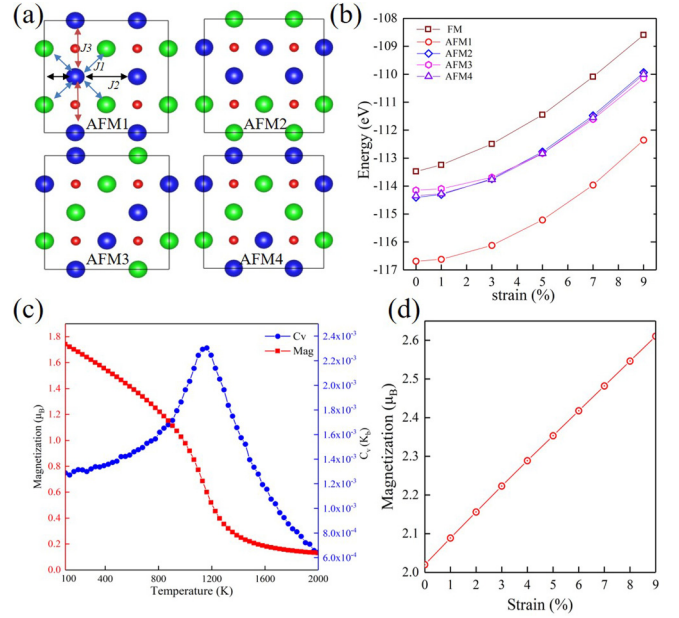


FIG. 2. (a) Four AFM configurations, AFM1, AFM2, AFM3, AFM4. Green and blue represent Mo atoms with opposite spins (green represents spin up, blue represents spin down), and red represents O atoms. J_1 is the nearest-neighbor coupling, and $J_{2/3}$ the next-nearest-neighboring coupling along the y/x direction. (b) Energy of ground states of different spin configurations for several different tensile stresses. (c) Evolution of specific heat capacity (C_v) and ionic magnetic moment with temperature. (d) Change of magnetic moment with tensile strain.

of the Supplemental Material (SM) [44]. Then a molecular dynamics simulation is performed at a temperature of 300 K with a 3×3 supercell. The numerical results shown in Fig. 1(e) show that the energy fluctuation is small in the time range of 1000 – $10\,000$ fs. It suggests that this structure is mechanically stable. Finally, we calculate the elastic constants of the structure. We have $C_{11} = 118.87$ N/m, $C_{33} = 0.68$ N/m, $C_{44} = 0.13$ N/m, $C_{66} = 34.70$ N/m, $C_{12} = 50.72$ N/m, $C_{13} = 0.14$ N/m, satisfying $C_{11} > |C_{12}|$, $C_{44}, C_{66} > 0$, $(C_{11} + C_{12})C_{33} > 2C_{13}^2$, which is the criterion of mechanical stability [45]. The phonon spectrum, elastic constants, and thermodynamic stability analyses are necessary for the stability of the crystal studied, though it may be not sufficient. All these positive results show that the MoO monolayer may be stable and fabricated in experiment.

Due to the exchange and correlation effect of $4d$ electrons in a Mo atom, the MoO monolayer lies in an antiferromagnetic phase. Each Mo atom has a magnetic moment of $2.02 \mu_B$ while the net moment vanishes over a unit cell. To confirm this point, we consider the possible spin distributions and have designed five different configurations, named FM, AFM1, AFM2, AFM3, and AFM4, to compare the ground state energy of these configurations. The first is a ferromagnetic configuration. The last four are antiferromagnetic configurations which are shown in Fig. 2(a), with blue and green representing opposite magnetic moments. The ground state energy is shown in Fig. 2(b) for these five configurations. The AFM1 configuration, which exhibits a collinear AFM

order, has been determined to be the ground state of the MoO monolayer, since it has the lowest energy. We have also studied the effect of biaxial tensile strain, which protects the symmetry of the structure. The results show that AFM1 is always the ground state in the range 0%–9%. Additionally, we have determined that the easy magnetic axis in the MoO monolayer is out of plane. This conclusion is supported by the calculation of the magnetic anisotropic energy (MAE), which is given by $\text{MAE} = E_x - E_z = 0.42 \text{ meV}$, in which $E_{x/z}$ represents the energy for magnetic moments aligned at the x/z direction.

To determine the Néel temperature of the AFM phase transition, we describe the spin system with the Heisenberg spin model. The Hamiltonian is given by

$$H = - \sum_{ij\alpha} J_{ij}^{\alpha} \hat{S}_i^{\alpha} \hat{S}_j^{\alpha} - D \sum_i (\hat{S}_i^z)^2, \quad (1)$$

where S_i^{α} is the α component of a spin vector on the i th Mo site, with $\alpha = (x, y, z)$. $J_{ij}^{x/y/z}$ describes the exchange coupling between spins aligned along the $x/y/z$ direction situated on sites i and j . D is the single-ion anisotropy. The first term is the classical Heisenberg model, and for simplicity, we have considered only the nearest- (J_1) and next-nearest (J_2, J_3)-neighboring couplings, as shown in Fig. 2(a). We have denoted the next-nearest coupling between two blue Mo cations along the y/x direction as $J_{2/3}$, respectively, since the coupling along the y direction is bridged by O anions, while it is the direct exchange along the x direction. The last term in Eq. (1) is to ensure the easy magnetic axis is out of plane. To determine the parameters in the model, we have calculated the energy of several spin configurations including FM, AFM1, AFM3, and AFM4 with a supercell of $2 \times 2 \times 1$. At the same time, these energies can also be expressed with the parameters in the model Hamiltonian directly,

$$E_{\text{FM}}^{\alpha} = E_0 - (16J_1^{\alpha} + 8J_2^{\alpha} + 8J_3^{\alpha})|\vec{S}|^2 - 8D|S^z|^2\delta_{\alpha,z}, \quad (2a)$$

$$E_{\text{AFM1}}^{\alpha} = E_0 + (16J_1^{\alpha} - 8J_2^{\alpha} - 8J_3^{\alpha})|\vec{S}|^2 - 8D|S^z|^2\delta_{\alpha,z}, \quad (2b)$$

$$E_{\text{AFM3}}^{\alpha} = E_0 - (-8J_2^{\alpha} - 8J_3^{\alpha})|\vec{S}|^2 - 8D|S^z|^2\delta_{\alpha,z}, \quad (2c)$$

$$E_{\text{AFM4}}^{\alpha} = E_0 + 8J_2^{\alpha}|\vec{S}|^2 - 8D|S^z|^2\delta_{\alpha,z}. \quad (2d)$$

Therefore, we can obtain these parameters as $J_1^z = -25.11 \text{ meV}$, $J_1^x = J_1^y = -25.29 \text{ meV}$, $J_2^z = 8.52 \text{ meV}$, $J_2^x = J_2^y = 7.92 \text{ meV}$, $J_3^z = 6.11 \text{ meV}$, $J_3^x = J_3^y = 6.92 \text{ meV}$, and $D = 0.18 \text{ meV}$. The decay of J_{ij} with distance is shown in Fig. S2 of the SM [44]. We have simulated this spin model with the classical Monte Carlo method. The results of specific heat capacity (C_v) and magnetic moment of each Mo atom have been obtained for several temperatures, as plotted in Fig. 2(c). A sharp peak of C_v and a rapid decrease of magnetic moment is observed at about $T_N \approx 1100 \text{ K}$, which is explained as the Néel temperature, denoting the phase transition from AFM to the paramagnetic phase. However, the value here suggests only qualitatively that the Néel temperature might be high in this system. To achieve a more precise Néel temperature, simulations of additional spin-spin couplings may be necessary [46].

In addition, we have also studied the effect of biaxial tensile strain on the magnetic moment. As shown in Fig. 2(d),

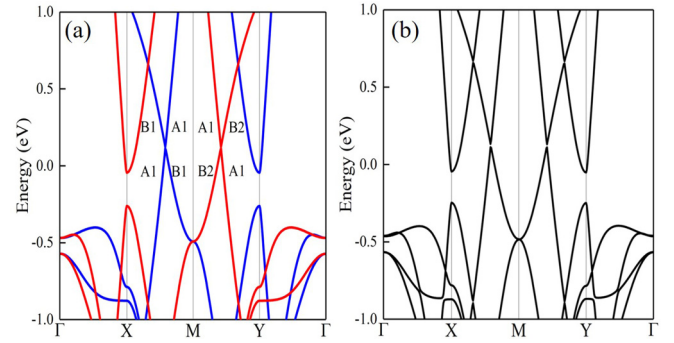


FIG. 3. Band structures of MoO (a) without SOC and (b) with SOC.

the magnetic moment exhibits a nearly linear increase with increasing strain. This behavior suggests that the magnetic moment becomes more localized as the strain is applied. It is consistent with the Hubbard model [47]. According to this model, as the lattice constant expands under strain, the hopping coefficient decreases relative to the on-site interaction. Consequently, the d electrons become more localized, resulting in an increase in the magnetic moment.

IV. ELECTRONIC PROPERTIES

We have calculated the electronic band structure of the MoO monolayer. The numerical results in the absence of spin-orbit coupling (SOC) are shown in Fig. 3(a). We find that it is a metal since the Fermi surface crosses both the conduction and valence bands. It is interesting that two bands cross each other on the boundary of the first Brillouin zone to form four Weyl points near the Fermi surface. The crossing, and therefore the Weyl points, are protected by spatial symmetry. Take the case of the M - X line as an example. The symmetry group of points on the M - X line is $C_{2v} = \{E, M_x, M_y, C_y\}$, which includes two vertical mirrors and a twofold axis along the y direction. The numerical analysis indicates that the irreducible representations of the bands are A_1 and B_1 , respectively, as labeled in Fig. 3(a). Therefore, the coupling between these two bands is forbidden, which results in the Weyl point. We also find that the bands on Γ - X - M have opposite spin compared with the bands on the Γ - Y - M line. The reason is that the crystal is unchanged after a fourfold rotation and time-reversal symmetry in the AFM phase.

In the presence of SOC, Weyl points are all gapped on the boundary. However, the SOC is not strong enough to result in a metal-insulator transition. It is doubtful whether it is a topological nontrivial phase, since there is a well-defined direct gap. To make it clear, it is necessary to tune the band structure to realize a global band gap, which can be realized by a biaxial tensile strain.

Figure 4 shows the effect of biaxial tensile strain on electronic bands. Strain will lower the valence band maximum (denoted as E_3) at the X point and Weyl points (E_1) on the boundary line, while the conduction band minimum (E_2) is raised gradually. The evolution is shown in Fig. 4(c). E_2 meets the Weyl point at a critical strain 2.6%. If the strain is larger, E_2 is lifted above the Fermi surface while the Weyl points (E_1) are pinned on the Fermi surface. The band with a strain

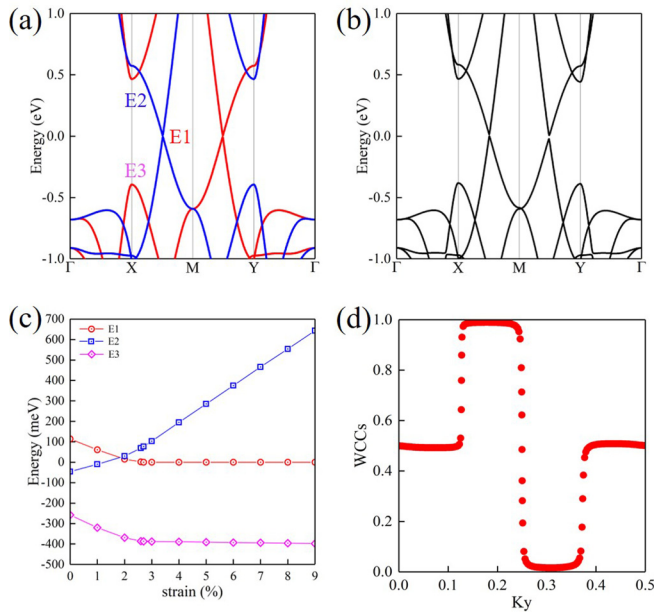


FIG. 4. Band structures (a) without SOC and (b) with SOC under a tensile strain of 7%. (c) The evolution of E_1 , E_2 , and E_3 [denoted in (a)] with tensile strains. (d) Wilson loop.

of 7% is shown in Fig. 4(a) without SOC. It is clear that strain leads to a metal-Weyl semimetal phase transition. If SOC is included, Weyl points are all gapped, as shown in Fig. 4(b). In this case, strain will lead to a metal-insulator phase transition. Here, we underline that the type of strain is essential to realize this phase transition. Further numerical results show that uniaxial strain cannot lead to a global band gap. This is also the case of the CrO monolayer [31,48].

The evolution of Wannier charge centers (WCCs) is commonly utilized to discern whether or not a system is topologically trivial. This can be accomplished by computing an effective one-dimensional system using the Wilson loop method [49,50], where k_y is treated as an adiabatic parameter. Figure 4(d) gives the WCCs. It indicates that the insulator phase is topologically trivial since a horizontal line crosses the loop two times. Further numerical results show that there always exists a direct gap for strain in the range of 0%–9% if SOC considered. Therefore, both the metal at small strain and insulator phases at large strain are topologically trivial. The vanishing Chern number is protected by an effective TRS which is a combination of TRS and a fourfold rotation about the z axis.

To realize the QAH effect, it is necessary to break the symmetry further. Therefore, we apply a shear strain to tune the electronic structure and we calculate that its ground state is still in the AFM1 configuration. Energy bands without and with SOC are shown in Figs. 5(a) and 5(b), respectively, with an angle of 89.5° between the two lattice bases in the horizontal plane. We find that Weyl points on the boundary line are gapped even in the absence of SOC, since the original symmetry operations, the mirror and rotation, are all broken. If SOC is considered, there is still a gap of about 50 meV to realize an insulator phase. We have calculated the Berry curvature $\Omega_z(\vec{k})$ of the occupied bands which can be expressed

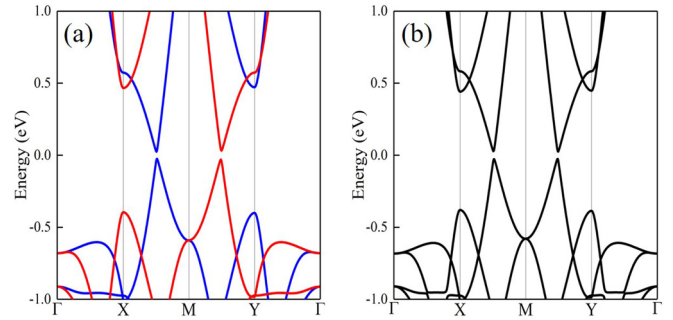


FIG. 5. Band structures (a) without SOC and (b) with SOC in the presence of both tensile strain (7%) and shear strain (89.5°).

as

$$\Omega_z(\vec{k}) = -2 \text{Im} \sum_{mn} \frac{\langle n\vec{k} | v_x | m\vec{k} \rangle \langle m\vec{k} | v_y | n\vec{k} \rangle}{(\omega_m - \omega_n)^2}, \quad (3)$$

where $\omega_{m/n}$ is the energy of the m/n th band, and $v_{x/y}$ denotes the velocity operator along the x/y direction. The numerical result, shown in Fig. 6(a), shows that the Berry curvature concentrates mainly around the gapped Weyl points across the Brillouin zone. We note that the Brillouin zone is still a square approximately, since the shear strain causes only a small deviation from the tetragonal lattice. The Berry phase is polarized with different strengths for the positive and negative valleys. Then we have calculated the anomalous Hall conductivity σ_H , which is given by

$$\sigma_H = -\frac{e^2}{h} \frac{1}{2\pi} \int_{\text{BZ}} \Omega_z(\vec{k}) d^2\vec{k}. \quad (4)$$

Integrating the Berry curvature $\Omega_z(\vec{k})$ over the Brillouin zone, we obtain a quantized Hall conductivity $-e^2/h$ in the gap regime as shown in Fig. 6(b). It indicates a nonzero Chern number $C = -1$. In addition, we have also calculated the edge state by the WANNIER90 software package. Results in Fig. 6(c) show that there is a single gapless chiral edge state connecting the conduction and valence bands, which is the result of bulk-edge correspondence. This quantum state can be detected by noncontact magneto-optical technology and is therefore critical for most practical applications, especially in two-dimensional devices.

V. CONCLUSIONS

In conclusion, we find that the MoO monolayer may be a metal if it can be prepared in a single-layer form, and a gap could open with both tensile and shear strains applied. Such a system would then be an AFM Chern insulator. The stability is verified by phonon spectra, molecular dynamics simulation, and elastic constants. A magnetic moment of larger than $2 \mu_B$ lies on each Mo atom and is distributed collinearly to form an AFM phase. Without SOC, it is a metal with Weyl points near the Fermi surface. With SOC, Weyl nodes are gapped to realize a metal phase with a direct gap across the Brillouin zone. Tensile strain will shift the conduction and valence bands to high energy, except for the Weyl points which will be pinned on the Fermi surface. SOC will gap the Weyl nodes and it becomes a trivial insulator. Shear strain will break the

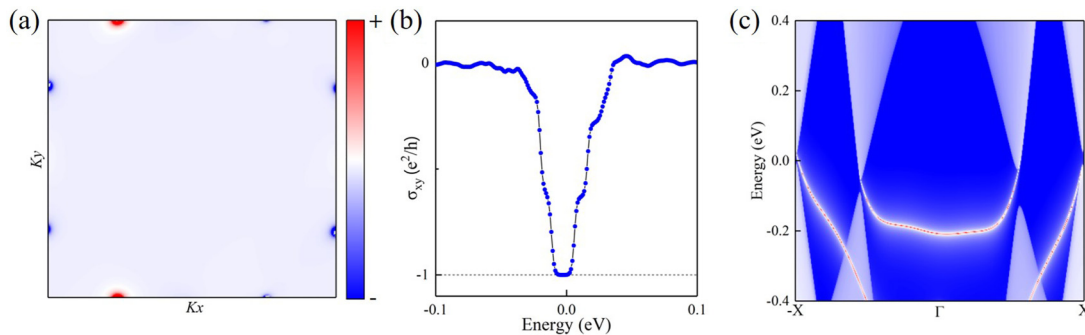


FIG. 6. (a) Berry curvature of occupied states. (b) Anomalous Hall conductivity vs chemical potential. (c) The energy spectrum of a half-infinite structure of the MoO monolayer.

effective time-reversal symmetry to realize a Chern insulator with $C = -1$. Our study reveals a scheme for implementing the QAH effect in AFM materials. In particular, once QAH insulators are implemented in AFM systems, one can observe QAH effects at near room temperature. As of now, neither MoO monolayers nor other similar materials have been experimentally synthesized, and we hope that our results will draw more attention to these systems by both theoretical and experimental communities.

ACKNOWLEDGMENTS

This work was supported by the National Natural Science Foundation of China (Grants No. 12104183, No. 52173283, and No. 62071200), the Natural Science Foundation of Shandong province (Grant No. ZR2021MA040), Taishan Scholar Program of Shandong Province (Grant No. ts20190939), and Independent Cultivation Program of Innovation Team of Jinan City (Grant No. 2021GXRC043).

[1] C. X. Liu, S. C. Zhang, and X. L. Qi, The quantum anomalous Hall effect: Theory and experiment, *Annu. Rev. Condens. Matter Phys.* **7**, 301 (2016).

[2] C. Z. Chang, C. X. Liu, and A. H. MacDonald, Quantum anomalous Hall effect, *Rev. Mod. Phys.* **95**, 011002 (2023).

[3] X. L. Qi, Y. S. Wu, and S. C. Zhang, General theorem relating the bulk topological number to edge states in two-dimensional insulators, *Phys. Rev. B* **74**, 045125 (2006).

[4] F. D. M. Haldane, Model for a Quantum Hall Effect without Landau Levels: Condensed-Matter Realization of the “Parity Anomaly”, *Phys. Rev. Lett.* **61**, 2015 (1988).

[5] C. Lei and A. H. MacDonald, Gate-tunable quantum anomalous Hall effects in MnBi₂Te₄ thin films, *Phys. Rev. Mater.* **5**, L051201 (2021).

[6] J. Zhang, C. Z. Chang, P. Tang, Z. Zhang, X. Feng, K. Li, L. L. Wang, X. Chen, C. Liu, W. Duan, K. He, Q. K. Xue, X. Ma, and Y. Wang, Topology-driven magnetic quantum phase transition in topological insulators, *Science* **339**, 1582 (2013).

[7] C. Z. Chang, P. Tang, Y. L. Wang, X. Feng, K. Li, Z. Zhang, Y. Wang, L. L. Wang, X. Chen, C. Liu, W. Duan, K. He, X. C. Ma, and Q. K. Xue, Chemical-Potential-Dependent Gap Opening at the Dirac Surface States of Bi₂Se₃ Induced by Aggregated Substitutional Cr Atoms, *Phys. Rev. Lett.* **112**, 056801 (2014).

[8] S. F. Zhang, H. Jiang, X. C. Xie, and Q. F. Sun, Effect of magnetic field on a magnetic topological insulator film with structural inversion asymmetry, *Phys. Rev. B* **89**, 155419 (2014).

[9] H. Polshyn, J. Zhu, M. A. Kumar, Y. Zhang, F. Yang, C. L. Tschirhart, M. Serlin, K. Watanabe, T. Taniguchi, A. H. MacDonald, and A. F. Young, Electrical switching of magnetic order in an orbital Chern insulator, *Nature (London)* **588**, 66 (2020).

[10] H. Sun, S. S. Li, W. X. Ji, and C. W. Zhang, Valley-dependent topological phase transition and quantum anomalous valley Hall effect in single-layer RuClBr, *Phys. Rev. B* **105**, 195112 (2022).

[11] D. Xiao, W. Zhu, Y. Ran, N. Nagaosa, and S. Okamoto, Interface engineering of quantum Hall effects in digital transition metal oxide heterostructures, *Nat. Commun.* **2**, 596 (2011).

[12] J. Wang, B. Lian, H. Zhang, Y. Xu, and S. C. Zhang, Quantum Anomalous Hall Effect with Higher Plateaus, *Phys. Rev. Lett.* **111**, 136801 (2013).

[13] Y. P. Wang, W. X. Ji, C. W. Zhang, P. Li, S. F. Zhang, P. J. Wang, S. S. Li, and S. S. Yan, Two-dimensional arsenene oxide: A realistic large-gap quantum spin Hall insulator, *Appl. Phys. Lett.* **110**, 213101 (2017).

[14] S. J. Zhang, C. W. Zhang, S. F. Zhang, W. X. Ji, P. Li, P. J. Wang, S. S. Li, and S. S. Yan, Intrinsic Dirac half-metal and quantum anomalous Hall phase in hexagonal metal-oxide lattice, *Phys. Rev. B* **96**, 205433 (2017).

[15] G. Xu, H. Weng, Z. Wang, X. Dai, and Z. Fang, Chern Semimetal and the Quantized Anomalous Hall Effect in HgCr₂Se₄, *Phys. Rev. Lett.* **107**, 186806 (2011).

[16] Y. T. Han, W. X. Ji, P. J. Wang, P. Li, and C. W. Zhang, Strain-tunable skyrmions in two-dimensional monolayer Janus magnets, *Nanoscale* **15**, 6830 (2023).

[17] X. Kou, S. T. Guo, Y. Fan, L. Pan, M. Lang, Y. Jiang, Q. Shao, T. Nie, K. Murata, J. Tang, Y. Wang, L. He, T. K. Lee, W. L. Lee, and K. L. Wang, Scale-Invariant Quantum Anomalous Hall Effect in Magnetic Topological Insulators beyond the Two-Dimensional Limit, *Phys. Rev. Lett.* **113**, 137201 (2014).

[18] S. S. Li, W. X. Ji, S. J. Hu, C. W. Zhang, and S. S. Yan, Effect of amidogen functionalization on quantum spin Hall effect in 2D Bi/Sb(111) films, *ACS Appl. Mater. Interfaces* **9**, 41443 (2017).

- [19] M. H. Zhang, C. W. Zhang, P. J. Wang, and S. S. Li, Prediction of high-temperature Chern insulator with half-metallic edge states in asymmetry-functionalized stanene, *Nanoscale* **10**, 20226 (2018).
- [20] M. Z. Hasan and C. L. Kane, Topological insulators, *Rev. Mod. Phys.* **82**, 3045 (2010).
- [21] X. L. Qi and S. C. Zhang, Topological insulators and superconductors, *Rev. Mod. Phys.* **83**, 1057 (2011).
- [22] C. X. Liu, X. L. Qi, X. Dai, Z. Fang, and S.-C. Zhang, Quantum Anomalous Hall Effect in $\text{Hg}_{1-y}\text{Mn}_y\text{Te}$ Quantum Wells, *Phys. Rev. Lett.* **101**, 146802 (2008).
- [23] R. Yu, W. Zhang, H. J. Zhang, S. C. Zhang, X. Dai, and Z. Fang, Quantized anomalous Hall effect in magnetic topological insulators, *Science* **329**, 61 (2010).
- [24] C. Z. Chang, J. Zhang, X. Feng, J. Shen, Z. Zhang, M. Guo, K. Li, Y. Ou, P. Wei, L. L. Wang, Z. Q. Ji, Y. Feng, S. Ji, X. Chen, J. Jia, X. Dai, Z. Fang, S. C. Zhang, K. He, Y. Wang *et al.*, Experimental observation of the quantum anomalous Hall effect in a magnetic topological insulator, *Science* **340**, 167 (2013).
- [25] Y. Deng, Y. Yu, M. Z. Shi, Z. Guo, Z. Xu, J. Wang, X. H. Chen, and Y. Zhang, Quantum anomalous Hall effect in intrinsic magnetic topological insulator MnBi_2Te_4 , *Science* **367**, 895 (2020).
- [26] M. Serlin, C. L. Tschirhart, H. Polshyn, Y. Zhang, J. Zhu, K. Watanabe, T. Taniguchi, L. Balents, and A. F. Young, Intrinsic quantized anomalous Hall effect in a moiré heterostructure, *Science* **367**, 900 (2020).
- [27] T. Li, S. Jiang, B. Shen, Y. Zhang, L. Li, Z. Tao, T. Devakul, K. Watanabe, T. Taniguchi, L. Fu, J. Shan, and K. F. Mak, Quantum anomalous Hall effect from intertwined moiré bands, *Nature (London)* **600**, 641 (2021).
- [28] X. Hu, Half-metallic antiferromagnet as a prospective material for spintronics, *Adv. Mater.* **24**, 294 (2012).
- [29] T. Jungwirth, X. Marti, P. Wadley, and J. Wunderlich, Antiferromagnetic spintronics, *Nat. Nanotechnol.* **11**, 231 (2016).
- [30] V. Baltz, A. Manchon, M. Tsoi, T. Moriyama, T. Ono, and Y. Tserkovnyak, Antiferromagnetic spintronics, *Rev. Mod. Phys.* **90**, 015005 (2018).
- [31] P. J. Guo, Z. X. Liu, and Z. Y. Lu, Quantum anomalous Hall effect in antiferromagnetism, *npj Comput. Mater.* **9**, 70 (2023).
- [32] X. Li, A. H. MacDonald, and H. Chen, Quantum anomalous Hall effect through canted antiferromagnetism, [arXiv:1902.10650](https://arxiv.org/abs/1902.10650).
- [33] K. Jiang, S. Zhou, X. Dai, and Z. Wang, Antiferromagnetic Chern Insulators in Noncentrosymmetric Systems, *Phys. Rev. Lett.* **120**, 157205 (2018).
- [34] G. Kresse and J. Hafner, *Ab initio* molecular-dynamics simulation of the liquid-metal-amorphous-semiconductor transition in germanium, *Phys. Rev. B* **49**, 14251 (1994).
- [35] P. E. Blöchl, Projector augmented-wave method, *Phys. Rev. B* **50**, 17953 (1994).
- [36] G. Kresse and J. Furthmüller, Efficient iterative schemes for *ab initio* total-energy calculations using a plane-wave basis set, *Phys. Rev. B* **54**, 11169 (1996).
- [37] J. P. Perdew, K. Burke, and M. Ernzerhof, Generalized Gradient Approximation Made Simple, *Phys. Rev. Lett.* **77**, 3865 (1996).
- [38] S. L. Dudarev, G. A. Botton, S. Y. Savrasov, C. J. Humphreys, and A. P. Sutton, Electron-energy-loss spectra and the structural stability of nickel oxide: An LSDA+U study, *Phys. Rev. B* **57**, 1505 (1998).
- [39] V. I. Anisimov, J. Zaanen, and O. K. Andersen, Band theory and Mott insulators: Hubbard U instead of Stoner I , *Phys. Rev. B* **44**, 943 (1991).
- [40] C. E. Calderon, J. J. Plata, C. Toher, C. Oses, O. Levy, M. Fornari, A. Natan, M. J. Mehl, G. Hart, M. Buongiorno Nardelli, and S. Curtarolo, The AFLOW standard for high-throughput materials science calculations, *Comput. Mater. Sci.* **108**, 233 (2015).
- [41] Q. Wu, S. Zhang, H. Song, M. Troyer, and A. A. Soluyanov, WANNIERTOOLS: An open-source software package for novel topological materials, *Comput. Phys. Commun.* **224**, 405 (2018).
- [42] A. A. Mostofi, J. R. Yates, Y. S. Lee, I. Souza, D. Vanderbilt, and N. Marzari, WANNIER90: A tool for obtaining maximally-localised Wannier functions, *Comput. Phys. Commun.* **178**, 685 (2008).
- [43] M. P. L. Sancho, J. M. L. Sancho, and J. Rubio, Highly convergent schemes for the calculation of bulk and surface Green functions, *J. Phys. F: Met. Phys.* **15**, 851 (1985).
- [44] See Supplemental Material at <http://link.aps.org/supplemental/10.1103/PhysRevB.107.214419> for electronic states for the MoO and CrO monolayers; phonon spectra of the MoO monolayer; decay of J_{ij} and six configurations; the energy of six configurations; magnetic excitation gap; and the energy band structure of the MoO monolayer under uniaxial tension.
- [45] F. Mouhat and F. X. Coudert, Necessary and sufficient elastic stability conditions in various crystal systems, *Phys. Rev. B* **90**, 224104 (2014).
- [46] J. Volny, K. Charvatova, M. Veis, V. Holy, M. Vondracek, J. Honolka, E. Duverger-Nedellec, J. Schusser, S. W. D'Souza, J. Minar, J. M. Pientka, A. Marmodoro, K. Vyborny, and K. Uhlirva, Single-crystal studies and electronic structure investigation of the room-temperature semiconductor NaMnAs, *Phys. Rev. B* **105**, 125204 (2022).
- [47] Z. Z. Li, *Solid State Theory*, 2nd ed. (Higher Education Press, Beijing, 2002).
- [48] X. Chen, D. Wang, L. Y. Li, and B. Sanyal, Room temperature two-dimensional antiferromagnetic Weyl semimetal CrO with giant spin-splitting and spin-momentum locked transport, [arXiv:2104.07390](https://arxiv.org/abs/2104.07390).
- [49] R. Yu, X. L. Qi, A. Bernevig, Z. Fang, and X. Dai, Equivalent expression of \mathbb{Z}_2 topological invariant for band insulators using the non-Abelian Berry connection, *Phys. Rev. B* **84**, 075119 (2011).
- [50] J. E. Padilha, L. B. Abdalla, A. J. R. da Silva, and A. Fazzio, Fully and partially iodinated germanane as a platform for the observation of the quantum spin Hall effect, *Phys. Rev. B* **93**, 045135 (2016).